A density-independent rigidity transition in biological tissues

Dapeng Bi[1], J. H. Lopez[1], J. M. Schwarz[1,2], and M. Lisa Manning[1,2]
[1]Department of Physics, Syracuse University, Syracuse, NY 13244, USA
[2]Syracuse Biomaterials Institute, Syracuse, NY 13244, USA

Cell migration is important in many biological processes, including embryonic development, cancer metastasis, and wound healing. In these tissues, a cell's motion is often strongly constrained by its neighbors, leading to glassy dynamics. While self-propelled particle models exhibit a density-driven glass transition, this does not explain liquid-to-solid transitions in confluent tissues, where there are no gaps between cells and therefore the density is constant. Here we demonstrate the existence of a new type of rigidity transition that occurs in the well-studied vertex model for confluent tissue monolayers at constant density. We find the onset of rigidity is governed by a model parameter that encodes single-cell properties such as cell-cell adhesion and cortical tension, providing an explanation for a liquid-to-solid transitions in confluent tissues and making testable predictions about how these transitions differ from those in particulate matter.

Important biological processes such as embryogensis, tumorigenesis, and wound healing require cells to move collectively within a tissue. Recent experiments suggest that when cells are packed ever more densely, they start to exhibit collective motion [1–3] traditionally seen in non-living disordered systems such as colloids, granular matter or foams [4–6]. These collective behaviors exhibit growing timescales and lengthscales associated with rigidity transitions.

Many of these effects are also seen in Self-Propelled Particle (SPP) models [7]. In SPP models, overdamped particles experience an active force that causes them to move at a constant speed, and particles change direction due to interactions with their neighbors or an external bath. To model cells with a cortical network of actomyosin and adhesive molecules on their surfaces, particles interact as repulsive disks or spheres, sometimes with an additional short-range attraction [8, 9]. These models generically exhibit a glass transition at a critical packing density of particles, ϕ_c, where $\phi_c < 1$ [1, 8, 10, 11], and near the transition point they exhibit collective motion [8] that is very similar to that seen in experiments [12].

An important open question is whether the density-driven glass transition in SPP models explains the glassy behavior observed in non-proliferating confluent biological tissues, where there are no gaps between cells and the packing fraction ϕ is fixed at precisely unity. For example, zebrafish embryonic explants are confluent three-dimensional tissues where the cells divide slowly and therefore the number of cells per unit volume remains nearly constant. Nevertheless, these tissues exhibit hallmarks of glassy dynamics such as caging behavior and viscoelasticity. Furthermore, ectoderm tissues have longer relaxation timescales than mesendoderm tissues, suggesting ectoderm tissues are closer to a glass transition, despite the fact that both tissue types have the same density [1]. This indicates that there should be an additional parameter controlling glass transitions in confluent tissues.

In this work, we study confluent monolayers using the vertex model [13–21], to determine how tissue mechanical response varies with single-cell properties such as adhesion and cortical tension. We find a new type of rigidity transition that is not controlled by the density, but instead by a dimensionless *target shape index* that is specified by single-cell properties. This rigidity transition possesses several hallmarks of a second-order phase transition, including growing length scales near the critical point and a critical scaling collapse. These findings provide a novel explanation for liquid-to-solid transitions in tissues that remain at constant density.

The vertex model, which agrees remarkably well with experimental data for confluent monolayers [13–21], approximates the monolayer as a collection of adjacent columnar cells. The mechanical energy of a single cell labeled 'i' is given by [14, 16]:

$$E_i = \beta_i (A_i - A_{i0})^2 + \xi_i P_i^2 + \gamma_i P_i. \qquad (1)$$

The first term results from a combination of 3D cell incompressibility and the monolayer's resistance to height fluctuations [15]. Then β_i is a *height elasticity*, and A_i and A_{i0} are the actual and preferred cell cross-sectional areas.

The second term in equation (1) models the active contractility of the actin-myosin subcellular cortex, with elastic constant ξ_i [14], and the last term represents an interfacial tension γ_i set by a competition between the cortical tension and the energy of cell-cell adhesion [18, 22] between two contacting cells. γ_i can be positive if the cortical tension is greater than the adhesive energy, or negative if the adhesion dominates. It is also possible to incorporate strong feedback between adhesion and cortical tension in this term [18, 23]. Since only the effective forces – the derivatives of the energy with respect to the degrees of freedom – are physically relevant, equation (1) can be rewritten: $E_i = \beta_i (A_i - A_{i0})^2 + \xi_i (P_i - P_{i0})^2$, where $P_{i0} = -\gamma_i/(2\xi_i)$ is an effective target shape index.

As discussed in [16], when all single-cell properties are equal ($\beta_i = \beta$, $\xi_i = \xi$, $A_{i0} = A_0$, $P_{i0} = P_0$), the total mechanical energy of a tissue containing N cells can be non-dimensionalized:

$$\varepsilon = \frac{1}{\beta A_0^2} \sum_i^N E_i = \sum_i \left[(\tilde{a}_i - 1)^2 + \frac{(\tilde{p}_i - p_0)^2}{r} \right], \qquad (2)$$

where $\tilde{a}_i = A_i/A_0$ and $\tilde{p}_i = P_i/\sqrt{A_0}$ are the rescaled shape functions for area and perimeter. $r = \beta A_0^2/\xi$ is the *inverse*

perimeter modulus and $p_0 = P_0/\sqrt{A_0}$ is the *target shape index* [24]; a regular hexagon corresponds to $p_0^{hex} = 2\sqrt{2}\sqrt[4]{3} \approx 3.72$ and a regular pentagon to $p_0^{pent} = 2\sqrt{5}(5-2\sqrt{5})^{1/4} \approx 3.81$.

In non-biological materials, bulk quantities such as shear/bulk modulus, shear viscosity and yield stress are often used to describe the mechanical response to external perturbations. However, cells are self-propelled and even in the absence of external forces, cells in confluent tissues regularly intercalate, or exchange neighbors [25, 26]. In an isotropic confluent tissue monolayer where mitosis (cell division) or apoptosis (cell death) are rare, cell neighbor exchange must happen through intercalation processes known as T1 transitions [27, 28], as illustrated in Fig. 4 (a). The mechanical response of the tissue is governed by the rate of cell rearrangements, and within the vertex model, the rate of T1 rearrangements is related to the amount of mechanical energy required to execute a T1 transition [28]. Therefore, we first study how these energy barriers change with single-cell properties encoded in the model parameters r and p_0.

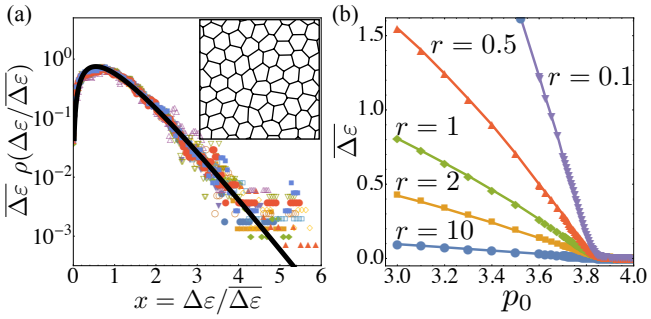

FIG. 1. **Energy barrier statistics.** (a) The normalized distribution ρ of normalized energy barrier heights $\Delta\varepsilon/\overline{\Delta\varepsilon}$ for a large range of parameters ($r = 0.5, 1, 2$ and $p_0 = 3.2 - 3.7$). They have a universal shape well-fit by a $k-$*gamma* distribution (solid line), indicating that $\overline{\Delta\varepsilon}$ completely specifies the distribution. (Inset) Snapshot of a typical simulated tissue with $r = 1$ and $p_0 = 3.5$. (b) $\overline{\Delta\varepsilon}$ as function of the target shape index p_0 for various values of the inverse perimeter modulus r.

To explore the statistics of energy barriers, we test all possible T1 transition paths (Methods) in 10 randomly generated samples each consisting of $N = 64$ cells. For each value of p_0 and r tested, we obtained the distribution of energy barrier heights $\rho(\Delta\varepsilon)$. The functional form of the distribution becomes universal (Fig. 1 (a)) when scaled by the mean energy barrier height $\overline{\Delta\varepsilon}(r, p_0)$. The rescaled distribution is well-fit by a $k-$*gamma* distribution ($k^k/(k-1)!\, x^{k-1}\exp(-kx)$) with $x = \Delta\varepsilon/\overline{\Delta\varepsilon}$ and $k = 2.2 \pm 0.2$. The $k-$*gamma* distribution has been observed in many non-biological systems disordered systems [29–31], and generically results from maximizing the entropy subject to constraints [30, 31]. This confirms that the distribution of energy barriers depends on the single-cell properties p_0 and r only through its average $\overline{\Delta\varepsilon}$.

A defining characteristic of a solid is that it possess a yield stress and a finite shear modulus, meaning it requires a finite amount of energy to deform. In the limit of vanishing cell motility, a tissue will be solid if there is a finite energy barrier to rearrangements, and it will flow otherwise. Fig. 1(b) is a plot of $\overline{\Delta\varepsilon}(r, p_0)$, the average mechanical energy cost of local T1 rearrangements, as function of p_0 at various values of r, showing that $\overline{\Delta\varepsilon}$ decreases as p_0 increases. At $p_0^* \sim 3.81$ the energy barrier vanishes, indicating that for p_0 larger than this value, deformation costs no energy and the vertex model becomes liquid-like. The inverse perimeter modulus r controls the scale of $\overline{\Delta\varepsilon}$ and the size of fluctuations in the perimeter.

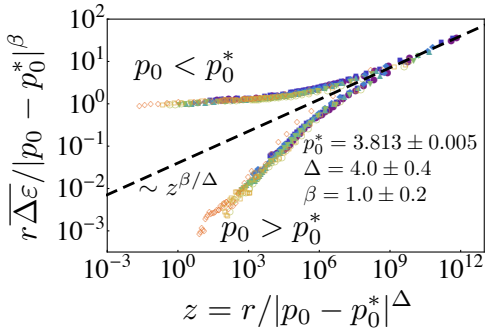

FIG. 2. Critical scaling collapse of the average energy barrier height $\overline{\Delta\varepsilon}$, normalized by $1/(r|p_0 - p_0^*|^\beta)$, as a function of $z = r/|p_0 - p_0^*|^\Delta$ for the data shown in Fig. 1(b), confirming the scaling ansatz of equation (3).

Fig. 1(b) is reminiscent of plots for the shear stress vs. the strain rate in particulate matter near the jamming transition [4, 32]. In these materials, the system loses mechanical rigidity as the packing fraction is decreased below a critical value. However, density can not control the rigidity transition in the vertex model because everything takes place at a packing fraction equal to unity. Instead, this model displays a novel rigidity transition controlled by the target shape index, p_0.

If the mechanical behavior of the tissue is truly controlled by a critical point at some p_0^*, then near the critical point the response $\overline{\Delta\varepsilon}$ should be related to the variable that controls the fluctuations r by a simple scaling ansatz:

$$r\,\overline{\Delta\varepsilon} = |p_0 - p_0^*|^\beta f_\pm\left(\frac{r}{|p_0 - p_0^*|^\Delta}\right). \qquad (3)$$

Here $z = r/|p_0 - p_0^*|^\Delta$ is the crossover scaling variable, Δ is the crossover scaling critical exponent, and f_-, f_+ are the two branches of the crossover scaling functions for $p_0 < p_0^*$ and $p_0 > p_0^*$, respectively [32].

After re-plotting the data in Fig. 1(b) using the scaling ansatz of equation (3), we find an excellent scaling collapse with $\Delta = 4.0 \pm 0.4$, $\beta = 1.0 \pm 0.2$ and $p_0^* = 3.813 \pm 0.005$ as shown in Fig. 2. This scaling collapse is similar to those seen in jamming in particulate matter [4, 32] and rigidity percolation on random networks [33–35], suggesting that p_0^* is a critical point analogous to Point J in the jamming transition

or the critical occupation probability p^* in random network models. For $p_0 < p_0^*$, as $z \to 0$, f_- is finite, which implies that the energy barrier $\overline{\Delta\varepsilon}$ scales as $(p_0^* - p_0)^\beta / r$. At $p_0 = p_0^*$, the two branches of the scaling function merge onto a common curve as $z \to \infty$, which has the power law scaling $z^{\beta/\Delta}$.

Although we calculate T1 transitions by shortening or lengthening a single cell-cell contact, our analysis of these local perturbations suggest a critical mechanical response with a growing lengthscale. To confirm and quantify these changes in the macroscopic mechanical response, we study the vibrational spectrum of the dynamical matrix [36, 37]. We diagonalize the dynamical matrix to obtain normal modes and their corresponding eigenvalues (Methods), which are the squares of the eigenfrequencies ω. The cumulative density of states is defined as the cumulative distribution function of ω,

$$N(\omega) = \int_{-\infty}^{\omega} D(\omega')d\omega' \tag{4}$$

where $D(\omega)$ is the density of states. If $N(\omega)$ remains finite as $\omega \to 0$, there are collective displacements of the vertices that cost zero energy and the system is a fluid, while if $N(\omega) \to 0$ as $\omega \to 0$, any linear combination of displacements costs finite energy and the material is a solid. Fig. 3 confirms our energy barrier results, showing a rigidity transition at $p_0 = p_0^* = 3.813$. For $p_0 < p_0^*$, N exhibits Debye scaling and approaches zero at zero frequency, while for $p_0 > p_0^*$, N exhibits a finite plateau at the lowest frequencies.

In addition, as the system approaches the rigidity transition from the solid phase, the density of states $D(\omega)$ exhibits a peak that shifts to lower frequencies, just as the so-called Boson Peak [37–39] in jammed particle packings and glasses. Interestingly, the shape and scaling of the peak is different from those in particulate matter, and this is an interesting avenue for future research.

Another important feature of a true second-order phase transition is the divergence of a correlation length at the crucial point. Static correlation length scales are notoriously difficult to identify in jammed particulate systems [32, 40, 41], and therefore we augment our static model with overdamped dynamics to study velocity-velocity correlation functions in response to point forces on the fluid side of the transition. In this numerical scheme, all cells in the system evolve according to

$$\frac{d\vec{r}_v}{dt} = -\frac{\partial \varepsilon}{\partial \vec{r}_v}. \tag{5}$$

We choose one cell at random, add a small additional constant force (magnitude 0.5) to the right hand side of Eq. 5, and measure a two-point equal time speed correlation function

$$c(r) = \left\langle \frac{v(r)}{v_1(0)} \right\rangle, \tag{6}$$

where $\langle ... \rangle$ denotes a time average and v_1 is the velocity of the particle with the additional force acting upon it. Fig. 3(b) is a plot of $c(r)$ over a range of p_0 values in the fluid regime,

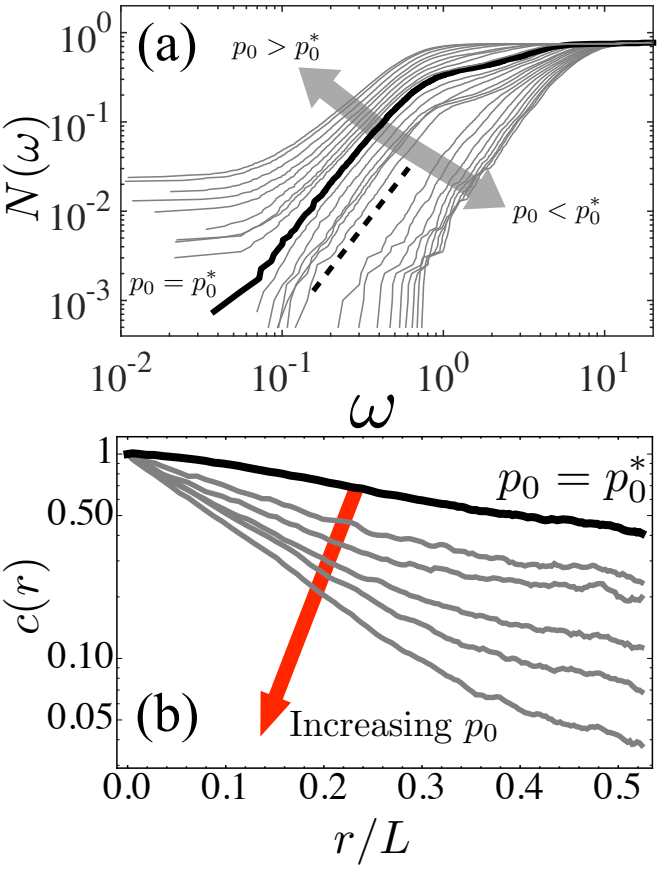

FIG. 3. (a) The cumulative vibrational density of states $N(\omega)$ exhibits a rigidity transition at $r = 1$ and $p_{0*} = 3.813$ (thick line). Thin lines correspond to $r = 1$ and values of p_0 ranging from 3.78 to 3.83 in increments of $10^{-}3$. Dashed line indicates power law of Debye scaling $\sim \omega^2$. (b) The two-point equal time velocity correlation $c(r)$ exhibits a growing lengthscale as $p_0 \to p_{0*}$ from above. From top to bottom, the lines represent: $p_0 = 3.813$(thick line), 3.818, 3.82, 3.85, 3.88, 3.9.

confirming that $c(r)$ exhibits a growing length scale as $p_0 \to p_0^*$ from above.

An obvious remaining question is what sets the critical point $p_0^* \sim 3.81$. To answer this question, we first study a simple mean-field model for a T1 topological swap. In an infinite confluent tissue, the topological Gauss-Bonnet theorem requires each cell to have six neighbors on average [27]. Therefore our mean-field model consists of four adjacent six-sided cells. To mimic the effect of additional neighboring cells, we fix each cell area equal to unity. Equation (2) then becomes:

$$\varepsilon_4 = \sum_{4\ cells} (\tilde{p}_i - p_0)^2; \quad a_i = 1. \tag{7}$$

Equation (7) is calculated numerically during a T1 rearrangement (Methods) as shown in Fig. 4(a). The total energy during this process is shown in Fig. 4(b) as the edge length ℓ is contracted (negative values) and a new edge is extended

(positive values); the energy barrier $\Delta\varepsilon$ is the difference in energy between the initial and maximum energy state. As p_0 increases, $\Delta\varepsilon$ decreases as shown in Fig. 4(c). The precise value p_0^* at which energy barriers vanish can be estimated by calculating the energy cost of shrinking an edge of length $\ell = \ell_0$ inside a hexagonal lattice, while all other edges remain unchanged. Precisely at the T1 transition, two of the cells are pentagons, while the other two remain hexagonal. Therefore if $p_0 < p_0^{pent} = \frac{7+2\sqrt{7}}{\sqrt{2}\times 3^{3/4}} \approx 3.812$, the transition necessarily drives the system away from the ground state, requiring finite energy. In contrast, for $p_0 \geq p_0^{pent}$ the cells are able to remain in the ground state throughout the transition, requiring zero energy. The estimate $p_0^* = p_0^{pent}$, indicated by a red dashed line in Fig. 4(c), does identify the critical target shape index in our mean-field model, and is consistent with the critical point $p_0^* = 3.813 \pm 0.005$ identified by the scaling collapse of energy barriers in the full vertex model.

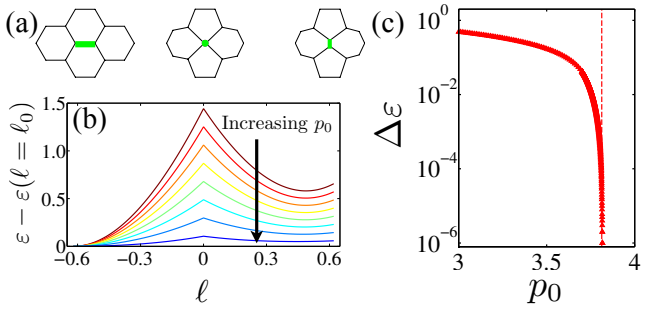

FIG. 4. (a) A four-cell aggregate undergoing a T1 topological swap. The thick (green) edge represents the cell-cell interface that is contracted to a point and then resolved in the perpendicular direction. (b) Energy of a four cell aggregate during a T1 transition, which attains a maximum at the transition point. p_0 varies from 1.5 to 3.8 in equal increments. (c) Energy barrier height as function of p_0 for a four-cell aggregate and a mean-field estimate (dashed) for the value of $p_0 = p_0^{pent}$ at which $\Delta\varepsilon$ vanishes.

Is there an even simpler explanation for $p_0^* \sim p_0^{pent}$? As in other rigidity transitions [6, 33, 34, 38], we expect that the critical shape index should also be related to isostaticity. In the vertex model with periodic boundary conditions, cells tile the flat 2D plane, and therefore the total number of vertices V, cells N, and edges E are related through Euler's formula: $0 = V - E + N$. Since each edge is shared by two cells, E is also related to the average coordination number z of cells or $E = Nz/2$, which yields $V = N(\frac{z}{2} - 1)$. The degrees of freedom are simply the motions of each vertex in 2D: $M_{dof} = 2V$. Assuming force balance (in both directions) and torque balance on each cell generates three constraints per cell: $M_c = 3N$. At isostaticity, the number of degrees of freedom equal the number of constraints: $M_{dof} = M_c$, resulting in $z_{iso} = 5$ and suggesting a mean-field transition at a shape index of $p_0^* \simeq 3.812$. Although it gives a correct prediction, this isostatic argument makes a strong assumption: that constraints are applied to each cell instead of to each vertex. Therefore, an interesting direction for future research is to understand under what circumstances the energy functional Eq. 2 effectively groups vertices into functional units that are cells.

We have shown that the vertex model, which has been used extensively to model tissues over the past 15 years, has a previously unreported critical rigidity transition with a diverging lengthscale that occurs at a critical value of the target shape index $p_0^* \sim 3.81$. This criticality is evident in (a) energy barriers to local T1 rearrangements, (b) the vibrational spectrum of the linear response, and (c) velocity-velocity correlations. Unlike SPP models where the liquid-to-solid transition is governed by density, our model has a constant-density glass transition governed by single-cell mechanical properties such as cell-cell adhesion and cortical tension encoded in the target shape index p_0.

Importantly, predictions based on this critical rigidity transition have recently been verified in biology experiments [42]. Specifically, in both simulations and experiments we can measure the shape index $p = P/\sqrt{A}$ for each cell in a monolayer, where P is the projected cell perimeter and A is the cross-sectional area. In simulations of the vertex model, we find that the median value of the observed shape index $\overline{p}$ is an order parameter that also exhibits critical scaling: $\overline{p} = p_0^* \sim 3.81$ for rigid or jammed tissues and $\overline{p}$ becomes increasingly larger than p_0^* as a tissue becomes increasingly unjammed. This prediction is precisely realized in cultures from primary cells in human patients, with implications for asthma pathobiology [42].

We expect that this rigidity framework will help biologists develop other testable hypotheses about how the mechanical response of tissues depends on single-cell properties. For example, Sadati *et al.* [43] have proposed a jamming phase diagram where tissues become more *solid-like* as adhesion increases, based on observations of jamming in adhesive particulate matter at densities far below confluency. Using standard interpretations of the vertex model (equations (1) and (2)), p_0 increases with increasing adhesion, and therefore our model predicts that confluent tissues become more *liquid-like* as adhesion increases. This highlights the fact that adhesion acts differently in particulate and confluent materials; in particulate matter higher adhesion leads to gelation and solidification, while in the vertex model larger adhesion leads to larger perimeters, more degrees of freedom, and liquid-like behavior. These ideas suggest that the role of adhesion in tissue rheology may be much richer and more interesting than previously thought.

In addition, although all published vertex models assume three-fold coordinated vertices, there is no proof that such structures are stable for $p_0 > p_0^{hex}$ [16]. Additionally, higher order vertices are apparently stabilized in some anisotropic biological tissues, including Rosette formation in Drosophila [44]. It will be interesting to study what conditions stabilize higher-fold vertices.

This work may also be relevant to modeling the Epithelial-to-Mesenchymal Transition (EMT) that occurs during cancer tumorigenesis. During EMT, epithelial cells with well-

defined, compact shapes and small perimeters relative to their areas transition to mesenchymal cells with irregular shapes and large perimeters relative to their areas [45]. Since equation (2) specifies a fixed shape index, one could interpret EMT as an increase in p_0 leading to a solid-to-liquid transition, providing a simple mechanical explanation for the role EMT plays in metastasis.

We expect that this model may be of interest to scientists independent of its biological relevance. We have shown it exhibits a simple rigidity transition with a novel control parameter, and therefore it might provide a useful bridge between jamming transitions in particulate matter [6, 38] and rigidity transitions in random elastic networks [33–35]. In particular, the potential grouping of vertices into functional cell units could draw an explicit connection between spring networks and particle/cell packings. An open question is whether our model belongs to an existing universality class, and whether the transition is mean-field.

A related issue is the question of ordered vs. disordered states. In this paper, we focus explicitly on disordered metastable states, but linear stability analysis predicts that the ground states exhibit an ordered-to-disordered transition at $p_0^{hex} \sim 3.722$ [16], instead of $p_0^* \approx p_0^{pent}$. Perhaps there are both "crystalline" and nonequilibrium "disordered" branches of the equation of state, with different transition points, just as in particulate matter [46]. Alternatively, linear stability analysis may not determine the transition point. A monte carlo study of ground states finds a transition at p_0^{pent} [47] and we also find that the linear response for a T1 transition (e.g. the quadratic curvature of $\varepsilon(\ell)$ in Fig. 4 (a)) vanishes at p_0^{hex}, but higher order terms still generate an energy barrier until p_0^{pent}.

Finally, the fact that the vertex model exhibits disordered ground states for $p_0 > p_0^*$ suggests that it may be a useful toy model for thermodynamic (as opposed to kinetic) explanations of the glass transition in particulate matter. Furthermore, these states are predicted to be hyperuniform [48] with a photonic band gap, indicating that they may be useful for designing metamaterials with interesting optical properties.

METHODS

Simulating a confluent tissue monolayer

To simulate confluent monolayers, a Random Sequential Addition point pattern [49] of N points was generated under periodic boundary conditions, with box size L chosen such that the average area per cell is unity. Two methods of generating this initial point pattern were used: a Random Sequential Addition point pattern [49], and a Poisson point pattern. The results presented in this work are independent of the method of initial point pattern generation. A voronoi tessellation of this point pattern results in a disordered cellular structure, which was then used as an input to the program *Surface Evolver* [50]. Surface Evolver numerically minimizes the total energy of the system (equation (2)) at fixed topology using gradient descent with respect to the vertices of the cells. If an edge shrinks below a threshold value l^*, a passive T1 transition is allowed if it lowers the energy. All structures are minimized such that the average energy of a cell changes by less than one part in 10^{10} between consecutive minimization steps, and as in other simulations of the vertex model [15, 16].

Once an initial energy-minimized state is reached, T1 transitions are actively induced at every edge to measure energy barriers [28]. An example of a T1 in the simple four-cell case is shown in Fig. 4(a): the central thick edge is quasi-statically contracted to zero length ($\ell = 0$) at which point a T1 topological swap is executed. After the T1, the length of the central edge is then expanded until it reaches the initial length ($\ell = \ell_0$). The total energy of four cells during this process is shown in Fig. 4(b); the edge length is represented by a negative value during contraction and flips sign after the T1.

For each active T1 transition in an N-cell system, the energy barrier is defined as the total energy difference between the initial state $\ell = \ell_0$ and the onset of T1 topological swap ($\ell = 0$). Calculations of energy barriers were repeated for various values of r at decade increments from 0.005 to 200 and p_0 ranging from 3 to 4.

Calculation of the vibration density of states

We obtain the vibrational density of states by diagonalizing the Hessian matrix of the system

$$H_{i\mu j\nu} = \frac{\partial^2 \varepsilon}{\partial r_{i\mu} r_{j\nu}}, \tag{8}$$

where i, j are indices for vertices and μ, ν cartesian coordinates, and ε is defined in Eq. (2). The eigenvalues of Eq. (8) are the squares of the eigenfrequencies ω.

Acknowledgements We would like to thank M. C. Marchetti for useful comments on this manuscript. M.L.M. acknowledges support from the Alfred P. Sloan Foundation, and M.L.M and D.B. acknowledge support from NSF-BMMB-1334611 and NSF-DMR-1352184. M.L.M and D.B. also would like to thank the KITP at the University of California Santa Barbara for hospitality and was supported in part by the National Science Foundation under Grant No. NSF PHY11-25915.

[1] Schoetz, E.-M., Lanio, M., Talbot, J. A. & Manning, M. L. Glassy dynamics in three-dimensional embryonic tissues. J. Roy. Soc. Interface **10**, 20130726 (2013).

[2] Angelini, T. E. et al. Glass-like dynamics of collective cell migration. Proceedings of the National Academy of Sciences **108**, 4714–4719 (2011).

[3] Nnetu, K. D., Knorr, M., Käs, J. & Zink, M. The impact of jamming on boundaries of collectively moving weak-interacting cells. New Journal of Physics **14**, 115012 (2012).

[4] Haxton, T. K., Schmiedeberg, M. & Liu, A. J. Universal jamming phase diagram in the hard-sphere limit. Phys. Rev. E **83**, 031503 (2011).

[5] Abate, A. R. & Durian, D. J. Topological persistence and dynamical heterogeneities near jamming. Phys. Rev. E **76**, 021306 (2007).

[6] Liu, A. J. & Nagel, S. R. The jamming transition and the marginally jammed solid. Annual Review of Condensed Matter Physics **1**, 347–369 (2010).

[7] Vicsek, T., Czirók, A., Ben-Jacob, E., Cohen, I. & Shochet, O. Novel type of phase transition in a system of self-driven particles. Phys. Rev. Lett. **75**, 1226–1229 (1995).

[8] Henkes, S., Fily, Y. & Marchetti, M. C. Active jamming: Self-propelled soft particles at high density. Phys. Rev. E **84**, 040301 (2011).

[9] Chate, H., Ginelli, F., Gregoire, G., Peruani, F. & Raynaud, F. Modeling collective motion: variations on the vicsek model. Eur. Phys. J. B **64**, 451–456 (2008).

[10] Berthier, L. Nonequilibrium glassy dynamics of self-propelled hard disks. Physical Review Letters **112**, 220602 (2014).

[11] Berthier, L. & Kurchan, J. Non-equilibrium glass transitions in driven and active matter. Nat Phys **9**, 310–314 (2013).

[12] Petitjean, L. et al. Velocity fields in a collectively migrating epithelium. Biophysical journal **98**, 1790–1800 (2010).

[13] Nagai, T. & Honda, H. A dynamic cell model for the formation of epithelial tissues. Philosophical Magazine Part B **81**, 699–719 (2001).

[14] Farhadifar, R., Rper, J.-C., Aigouy, B., Eaton, S. & Jlicher, F. The influence of cell mechanics, cell-cell interactions, and proliferation on epithelial packing. Current Biology **17**, 2095 – 2104 (2007).

[15] Hufnagel, L., Teleman, A. A., Rouault, H., Cohen, S. M. & Shraiman, B. I. On the mechanism of wing size determination in fly development. Proceedings of the National Academy of Sciences **104**, 3835–3840 (2007).

[16] Staple, D. B. et al. Mechanics and remodelling of cell packings in epithelia. Eur. Phys. J. E **33**, 117–127 (2010).

[17] Hilgenfeldt, S., Erisken, S. & Carthew, R. W. Physical modeling of cell geometric order in an epithelial tissue. Proceedings of the National Academy of Sciences **105**, 907–911 (2008).

[18] Manning, M. L., Foty, R. A., Steinberg, M. S. & Schoetz, E.-M. Coaction of intercellular adhesion and cortical tension specifies tissue surface tension. Proceedings of the National Academy of Sciences **107**, 12517–12522 (2010).

[19] Wang, G., Manning, M. L. & Amack, J. D. Regional cell shape changes control form and function of kupffer's vesicle in the zebrafish embryo. Developmental Biology **370**, 52–62 (2012).

[20] Chiou, K. K., Hufnagel, L. & Shraiman, B. I. Mechanical stress inference for two dimensional cell arrays. PLoS Comput Biol **8**, e1002512 (2012).

[21] Fletcher, A. G., Osterfield, M., Baker, R. E. & Shvartsman, S. Y. Vertex models of epithelial morphogenesis. Biophysical Journal **106**, 2291–2304.

[22] Graner, F. & Glazier, J. A. Simulation of biological cell sorting using a two-dimensional extended potts model. Physical Review Letters **69**, 2013–2016 (1992).

[23] Amack, J. D. & Manning, M. L. Extending the differential adhesion hypothesis in embryonic cell sorting. Science **338**, 212–215 (2012).

[24] In this Letter we focus on the regime where $p_0 > 0$, but $p_0 < 0$ is a valid parameter regime where our results hold as well.

[25] Lecuit, T. "developmental mechanics": Cellular patterns controlled by adhesion, cortical tension and cell division. HFSP Journal **2**, 72–78 (2008).

[26] Guillot, C. & Lecuit, T. Mechanics of epithelial tissue homeostasis and morphogenesis. Science **340**, 1185–1189 (2013).

[27] Weaire, D. L. & Hutzler, S. The physics of foams (Oxford University Press, 1999).

[28] Bi, D., Lopez, J. H., Schwarz, J. M. & Manning, M. L. Energy barriers and cell migration in densely packed tissues. Soft Matter **10**, 1885–1890 (2014).

[29] Newhall, K. A., Jorjadze, I., Vanden-Eijnden, E. & Brujic, J. A statistical mechanics framework captures the packing of monodisperse particles. Soft Matter **7**, 11518–11525 (2011).

[30] Aste, T. & Di Matteo, T. Emergence of gamma distributions in granular materials and packing models. Phys. Rev. E **77**, 021309 (2008).

[31] Bi, D., Zhang, J., Behringer, R. P. & Chakraborty, B. Fluctuations in shear-jammed states: A statistical ensemble approach. EPL (Europhysics Letters) **102**, 34002 (2013).

[32] Olsson, P. & Teitel, S. Critical scaling of shear viscosity at the jamming transition. Phys. Rev. Lett. **99**, 178001 (2007).

[33] Das, M., Quint, D. A. & Schwarz, J. M. Redundancy and cooperativity in the mechanics of compositely crosslinked filamentous networks. PLoS ONE **7**, e35939 (2012).

[34] Broedersz, C. P., Mao, X., Lubensky, T. C. & MacKintosh, F. C. Criticality and isostaticity in fibre networks. Nature Physics **7**, 983–988 (2011).

[35] Heussinger, C. & Frey, E. Floppy modes and nonaffine deformations in random fiber networks. Physical review letters **97**, 105501 (2006).

[36] Ashcroft, N. & Mermin, N. Solid State Physics. HRW international editions (Holt, Rinehart and Winston, 1976).

[37] Silbert, L. E., Liu, A. J. & Nagel, S. R. Vibrations and diverging length scales near the unjamming transition. Phys. Rev. Lett. **95**, 098301 (2005).

[38] Wyart, M., Silbert, L. E., Nagel, S. R. & Witten, T. A. Effects of compression on the vibrational modes of marginally jammed solids. Phys. Rev. E **72**, 051306 (2005).

[39] Manning, M. L. & Liu, A. J. A random matrix definition of the boson peak. Euro. Phys. Lett. (2013). arXiv:1307.5904.

[40] Tighe, B. P., Woldhuis, E., Remmers, J. J. C., van Saarloos, W. & van Hecke, M. Model for the scaling of stresses and fluctuations in flows near jamming. Phys. Rev. Lett. **105**, 088303 (2010).

[41] Mailman, M. & Chakraborty, B. A signature of a thermodynamic phase transition in jammed granular packings: growing correlations in force space. Journal of Statistical Mechanics: Theory and Experiment **2011**, L07002 (2011).

[42] Park, J.-A. et al. Unjamming transition to cellular hypermobility in the asthmatic airway epithelium (2015).

[43] Sadati, M., Qazvini, N. T., Krishnan, R., Park, C. Y. & Fredberg, J. J. Collective migration and cell jamming. Differentiation **86**, 121 – 125 (2013). Mechanotransduction.

[44] Kasza, K. E., Farrell, D. L. & Zallen, J. A. Spatiotemporal control of epithelial remodeling by regulated myosin phosphorylation. Proc Natl Acad Sci U S A **111**, 11732–11737 (2014).

[45] Kalluri, R., Weinberg, R. A. et al. The basics of epithelial-mesenchymal transition. The Journal of clinical investigation **119**, 1420–1428 (2009).

[46] Debenedetti, P. G. & Stillinger, F. H. Supercooled liquids and the glass transition. Nature **410**, 259–267 (2001).

[47] Hočevar, A. & Ziherl, P. Degenerate polygonal tilings in simple

animal tissues. Phys. Rev. E **80**, 011904 (2009).

[48] Gabrielli, A. & Torquato, S. Voronoi and void statistics for superhomogeneous point processes. Phys. Rev. E **70**, 041105 (2004).

[49] Torquato, S., Author & Haslach, H., Jr. Random heterogeneous materials: Microstructure and macroscopic properties. Applied Mechanics Reviews **55**, B62–B63 (2002).

[50] Brakke, K. A. The surface evolver. Experimental mathematics **1**, 141–165 (1992).